

On the Subclasses in *Swift* Long Gamma-Ray Bursts: A Clue to Different Central Engines

Ryo TSUTSUI¹, & Toshikazu SHIGEYAMA¹

¹*Research Center for the Early Universe, School of Science, University of Tokyo, Bunkyo-ku, Tokyo
113-0033, Japan*

(Received ; accepted)

Abstract

Analyzing light curves of a complete sample of bright *Swift* long gamma-ray bursts (LGRBs) of which the peak photon fluxes constructed with the bin width of 1 second in the *Swift* 15-350 keV energy band exceed 2.6 photons cm⁻²s⁻¹, we confirm that there do exist the third class in GRBs in addition to short and long GRBs. Being different from previous works based on the duration, fluence, etc. our classification method is based on two properties both quantified with light curve shapes of the prompt emission: *the Absolute Deviation from the Constant Luminosity of their cumulative light curve ADCL*, and *the ratio of the mean counts to the maximum counts \bar{C}/C_{\max}* . These are independent of the distance and the jet opening angle. A cluster analysis via the Gaussian mixture model detects three subclasses: one consisting of LGRBs with small *ADCL* and large \bar{C}/C_{\max} values referred to as Type I, one with large *ADCL* and large \bar{C}/C_{\max} referred to as Type II, and one with intermediate *ADCL* and small \bar{C}/C_{\max} , which is composed of contaminating short GRBs with the extended emission. This result is reinforced by different temporal and spectral indices of their X-ray afterglows. The difference is prominent in the temporal index of the steep decay phase in particular: the indices for Type I LGRBs distribute between -6 and -3 while those for Type II LGRBs between -3 and -2 . From these properties, we propose a possible scenario with different central engines: an accreting black hole and a magnetar.

Key words: gamma rays bursts : general — methods: observational — methods: statistical

1. Introduction

The existence of the third class of gamma-ray bursts (GRBs) has been studied by some authors. Nevertheless, it is not widely accepted unlike short and long GRBs (SGRBs and LGRBs). Horváth (1998) proposed the intermediate class of GRBs, because three log-normal

functions are needed to reproduce the distribution of durations T_{90} based on the BATSE data. This feature of the distribution was confirmed by the *Swift* data (Horváth et al. 2008) and *BeppoSAX* data (Horváth 2009). Some authors have searched better methods to classify the intermediate class more significantly with multi-dimensional analyses of burst properties such as the duration, spectral hardness, and fluence (Mukherjee et al. 1998; Hakkila et al. 2003; Horváth et al. 2006; Horváth et al. 2010), and confirmed the "intermediate" class.

Hakkila et al. (2000), however, insisted that the fluence and the duration of some faint long bursts are underestimated due to the background of detectors and that this bias could be responsible for such apparent characteristics of the intermediate class. Thus the existence of the third class has not been settled.

The purpose of this paper is to confirm the third class of GRBs with a completely different method from the previous works (Horváth 1998; Mukherjee et al. 1998; Hakkila et al. 2000; Horváth et al. 2010). In these works, the duration, hardness and/or fluence were used to classify GRBs, but these observed values include some obstacles to identifying the difference between subclasses of GRBs as follows:

- fluence - duration bias
- different intrinsic criteria for the truncation of GRBs at different distances and redshifts with the same detector limit
- different jet opening angles

Recently, Kocevski (2012) quantitatively estimated the effect of the bias on bursts exhibiting a single Fast Rise Exponential Decay (FRED) shape pulse by performing Monte Carlo simulations and concluded that a burst with the signal-to-noise ratio less than ~ 25 significantly suffers from the bias. As a consequence, it can conceal the expected time dilation due to the cosmological expansion. Besides these detector limit problems, the dependence of the duration and fluence on nuisance parameters, e.g., the distance, jet opening angle of a burst, makes the situation more complex. To establish the third class of GRBs, a new method free from these obstacles is inevitable.

There seem to be two possible ways to achieve our purpose here. The first is to make proper corrections to obtain only intrinsic properties of GRBs (Frail et al. 2001; Bloom et al. 2003; Ghirlanda et al. 2004). This approach needs information on the afterglow emission and the host galaxy in addition to the prompt emission and thus the number of sample with sufficient information significantly decreases. Furthermore, this approach needs to estimate the value of the jet opening angle by detecting an achromatic break in the afterglow emission predicted by the standard fireball model (Rhoads 1999). Therefore the discovery of chromatic breaks in the afterglow emission has brought this approach into a crisis (Panaitescu et al. 2006).

Here we propose an alternative way to extract properties independent of these nuisance parameters from observed light curves. In addition, we avoid the fluence - duration bias by

using bright LGRBs.

We use two properties to detect subgroups in our sample: the absolute deviation from the constant luminosity of their cumulative light curve $ADCL$ and the ratio of the mean photon counts to the maximum photon counts \bar{C}/C_{\max} . The first parameter is developed by Tsutsui et al. (2013) to show that there are two tight fundamental planes, rather than a single wide plane¹ (Tsutsui et al. 2009). The cumulative light curve of each event is constructed from the photon counts normalized with the total counts as a function of time normalized with T_{90} to eliminate the dependence on nuisance parameters. The second one is a new parameter introduced to classify LGRBs into subgroups more effectively and to avoid contamination of SGRBs with extended emission (SGRBwEE).

Here we show that a cluster analysis via the Gaussian mixture model detects two subclasses: Type I LGRB and Type II LGRB. Furthermore, this analysis identifies SGRBwEE creeping into the sample. We also investigate X-ray afterglow emission of LGRBs and find different properties in each type. Although most of them share a common canonical light curve in their X-ray afterglows, the slope of the steep decay phase for Type I LGRBs is steeper than that of Type II LGRBs. Furthermore, the spectra of Type I LGRBs are slightly softer than those of Type II LGRBs. The existence of the third class of LGRBs therefore are confirmed from properties of not only the prompt emission but also the X-ray afterglow emission.

Taking into account our results, we propose that the two subclasses have different central engines: an accreting black hole engine for Type I LGRBs and a magnetar engine for Type II LGRBs. The slower decay in the steep decay phase of Type II LGRBs might come from the temporal change of the magnetic dipole radiation due to the spin down of a magnetar. Furthermore the common shallow to normal phase might indicate that these two phases come from a common physical process independent of energy injection from central engines such as interactions with the circumstellar matter (Shigeyama & Tsutsui in prep).

In the next section, we explain how we select the sample. We classify LGRBs using the selected data of prompt emission in section 3 and X-ray afterglow emission in section 4. We discuss a possible connection of different properties found in the prompt emission and the X-ray afterglow emission of different classes of GRBs with the central engines in section 5. We make concluding remarks in section 6.

2. Selection criteria

Swift has monitored the sky since November 2004 and detected 769 GRBs up to 28 May 2013. It has three instruments to detect the prompt emission of GRBs and observe their afterglow emission in gamma-ray, X-ray, and ultraviolet/optical bands. After the Burst

¹ The fundamental plane is a correlation between the spectral peak energy (E_p), peak luminosity (L_p) and luminosity time (T_L), the total energy (E_{iso}) divided by the peak luminosity. Well known E_p - E_{iso} (Amati et al. 2002) and E_p - L_p (Yonetoku et al. 2004) correlations are projections of the fundamental plane.

Alert Telescope BAT (Barthelmy et al. 2005) detects the prompt emission of a GRB, *Swift* automatically slews in the direction of the GRB and starts the follow up observation with the X-Ray Telescope XRT (Burrows et al. 2005) and the Ultraviolet/Optical Telescope UVOT (Roming et al. 2005). Although there have been some other missions that detected a larger number of GRBs than *Swift*, these missions did not cover most GRBs in X-ray and optical bands or measure the redshifts. These pieces of information would help us to investigate the nature of GRBs from various viewpoints. Thus we analyze exclusively the GRBs detected by *Swift* in this paper.

From the *Swift* GRB table on the Web², we obtain the list of LGRBs including the trigger number, the duration T_{90}^{Swift} for which 90 % of the total photons of the event in the *Swift* 15-350 keV band are detected, the peak photon flux P in the *Swift* 15-150 keV band, the time $T_{\text{start}}^{\text{XRT}}$ elapsed from the BAT trigger to the first XRT observation, the initial temporal decay index α_{init} , and spectral index β_{XRT} obtained by XRT observations. The table contains 672 LGRBs up to 28 May 2013. From these 672 LGRBs, we excluded bursts not detected by onboard analyses and those with only the lower limit of T_{90}^{Swift} , and then the number of the sample decreases to 648. Because it is difficult to determine the correct duration and fluence of GRBs for dim events with the signal-to-noise ratio less than ~ 25 due to the fluence - duration bias (Kocevski 2012), we select events with the peak flux P in excess of 2.6 photons $\text{cm}^{-2} \text{s}^{-1}$. This criterion reduces the number of the appropriate events from 648 to 168. According to Salvaterra et al. (2012), this threshold flux corresponds to an instrument ~ 6 times less sensitive than *Swift*. Although the burst trigger threshold of the BAT detector is not simple, it is ranging from 4 to 11 σ above the background noise level with a typical value of 8 σ ³. From these facts, we consider that our criteria are sufficient to correctly determine the duration.

For these 168 events, we derive the durations T_{90}^{ours} 's by ourselves via the bayesian block algorithm from light curves in the *Swift* 15-350 keV band constructed with the bin size of 64 ms in the observer frame. To construct light curves, we use the `batgrbproduct` and `batbinevt` tools in the `heasoft` version 6.13 according to the instruction on the Web⁴. The correlation between T_{90}^{Swift} and T_{90}^{ours} is shown in Figure 1. For most of events, T_{90}^{ours} 's are consistent with T_{90}^{Swift} , which indicates our estimation of T_{90}^{ours} is reasonable. There are some outliers in Figure 1 probably because of the updated energy calibration of the BAT detector. We derive T_{90} by ourselves because we need to decide the starting time of T_{90} , which is not contained in the *Swift* GRB table, to calculate the two important parameters introduced in the next paragraph. We use the distributions of GRBs with respect to these parameters to investigate the subclasses.

We calculate two parameters from these light curves. The first is the absolute deviation from the constant luminosity of their cumulative light curves *ADCL* introduced in the previous

² http://swift.gsfc.nasa.gov/docs/swift/archive/grb_table.html/

³ http://heasarc.gsfc.nasa.gov/docs/swift/about_swift/bat_desc.html

⁴ <http://grbworkshop.wikidot.com/s9-10-swift-bat>

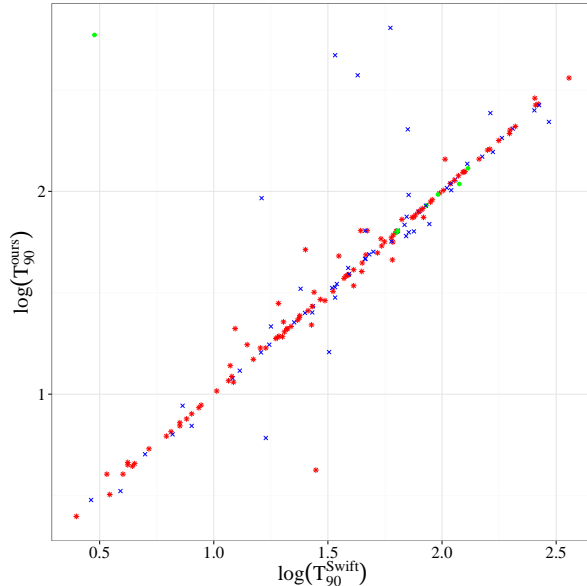


Fig. 1. The relationship between T_{90}^{Swift} and T_{90}^{ours} . Red points indicate Type I, Blue points Type II, and green points SGRBwEE. For the classification of GRBs, see section 3.

section. To define $ADCL$, we first calculate the normalized time $t_i^{\text{norm}} \equiv (t_i - t_{\text{start}}^{T_{90}})/T_{90}$ and normalized cumulative counts $C_i^{\text{cum}} \equiv (\sum_{k=1}^i C_k)/C_{\text{total}}$, where t_i (C_i), $t_{\text{start}}^{T_{90}}$ and C_{total} are the time (counts) of the i -th bin, the starting time of T_{90} , and the total counts, respectively. Both the normalized time and the normalized cumulative counts run from 0 to 1. From these normalized cumulative light curves, the definition of $ADCL$ is given by

$$ADCL = \sum_{i=1}^{N_{\text{bin}}} \frac{|C_i^{\text{cum}} - t_i^{\text{norm}}|}{N_{\text{bin}}}, \quad (1)$$

where the number N_{bin} of bins are different from burst to burst.

The other parameter \bar{C}/C_{max} is the ratio of the mean counts during the period T_{90}^{ours} , $\bar{C} = \sum C_i/N_{\text{bin}}$, to the maximum counts C_{max} . $(\bar{C}/C_{\text{max}})^{-1}$ can be regarded as an index sensitive to a kind of variability, although it is much simpler than the original definition (Fenimore & Ramirez-Ruiz 2000; Reichart et al. 2001).

We summarized the data in table 1.

Table 1. List of LGRBs.

	Trigger	$T_{90}^{\text{Swift}*}$	$T_{90}^{\text{ours}*}$	P_{\dagger}	$T_{\text{start}}^{\text{XRT}*}$	α_{init}	β_{XRT}	$ADCL$	$\log(\bar{C}/C_{\text{max}})$	Type
130528A	556870	59.40	640.00	3.00	64.87	-1.45	1.91	0.42	-1.62	Type II
130527A	556753	44.00	64.00	20.10	105.24	-1.50	1.67	0.21	-1.10	Type I
130514A	555821	204.00	203.90	2.80	88.83	-2.02	2.06	0.20	-0.83	Type II
130505A	555163	88.00	68.99	30.00	96.37	0.64	1.92	0.36	-1.26	Type II
130502A	554996	3.00	590.72	2.90	91.41	-0.68	2.21	0.03	-2.41	SGRBwEE
130427B	554635	27.00	25.28	3.00	77.37	-1.71	1.81	0.30	-0.83	Type II
130427A	554620	162.83	243.26	331.00	140.19	-2.79	1.79	0.36	-1.43	Type II
130420A	553977	123.50	124.16	3.40	735.33	-0.75	2.30	0.14	-0.68	Type I
130408A	553132	28.00	4.22	4.90	149.89	-0.47	2.03	0.06	-0.49	Type I
130216A	548927	6.50	6.53	6.50	317700.00			0.05	-0.26	Type I
121209A	540964	42.70	373.63	3.40	91.98	0.61	2.30	0.48	-1.77	Type II
121128A	539866	23.30	23.17	12.90	77.17	-2.37	1.99	0.12	-0.68	Type I
121125A	539563	52.20	49.73	2.90	66.80	-2.69	2.15	0.05	-0.55	Type I
121017A	536172	4.20	4.61	3.30	95.25	-0.96	2.14	0.08	-0.48	Type I
120918A	534015	25.10	25.15	4.50				0.19	-0.66	Type II
120913B	533613	126.00	125.38	3.20				0.05	-0.61	Type I
120911A	533268	17.80	21.57	2.70	3333.20	-1.24	2.02	0.23	-0.85	Type II
120907A	532871	16.90	6.08	2.90	82.02	-0.45	1.82	0.17	-0.51	Type II
120811C	530689	26.80	21.95	4.10	68.67	-4.62	1.92	0.09	-0.45	Type I
120802A	529486	50.00	50.37	3.00	84.78	-2.79	2.04	0.25	-0.93	Type II
120729A	529095	71.50	62.85	2.90	68.12	-1.12	1.88	0.27	-0.89	Type II
120703A	525671	25.20	51.58	10.50	86.73	-0.67	2.00	0.19	-1.19	Type I
120327A	518731	62.90	63.42	3.90	75.61	-2.96	1.76	0.10	-0.87	Type I
120326A	518626	69.60	60.16	4.60	59.54	-3.61	1.86	0.30	-0.93	Type II
120324A	518507	118.00	119.42	5.90	75.13	1.50	2.06	0.10	-0.97	Type I
120311A	517469	3.50	3.20	3.20	3161.63	-1.02	2.00	0.11	-0.53	Type I
120308A	517234	60.60	45.95	6.00	92.63	-3.62	1.65	0.04	-0.63	Type I
120218A	515277	27.50	31.81	9.10				0.10	-0.82	Type I
120119A	512035	253.80	250.88	10.30	53.29	-2.57	1.61	0.40	-1.19	Type II
120116A	511866	41.00	34.24	4.10	74.40	-3.99	2.09	0.10	-0.48	Type I
120102A	510922	38.70	38.59	10.30	112.94	-3.05	2.02	0.21	-0.99	Type I
111228A	510649	101.20	101.06	12.40	145.07	-5.45	2.04	0.11	-1.09	Type I
111121A	508161	119.00	108.74	7.10		-1.85	1.90	0.24	-1.88	SGRBwEE
111103B	506903	167.00	156.42	7.20		-3.07	1.87	0.30	-1.17	Type II
111103A	506902	11.60	11.65	3.10				0.05	-0.63	Type I

Table 1. (Continued.)

111008A	505054	63.46	63.30	6.40		-3.27	1.94	0.22	-0.99	Type II
110915A	503219	78.76	79.17	3.30		-6.09	2.25	0.08	-0.72	Type I
110731A	458448	38.80	41.92	11.00		1.29	1.85	0.38	-1.01	Type II
110715A	457330	13.00	13.06	53.90		-0.57	1.85	0.30	-0.79	Type II
110709A	456939	44.70	44.35	6.20		-1.41	2.06	0.04	-0.52	Type I
110625A	456073	44.50	40.26	49.50	140.35	-1.12	1.37	0.14	-0.93	Type I
110610A	455155	46.40	48.64	4.20	71.85	-2.84	2.29	0.06	-0.66	Type I
110519A	453628	27.20	27.14	4.60				0.18	-0.46	Type II
110422A	451901	25.90	25.79	30.70	814.50	-1.02	1.89	0.05	-0.34	Type I
110420A	451757	11.80	13.82	14.00	87.60	-3.98	2.05	0.07	-0.42	Type I
110402A	450545	60.90	56.26	4.10	544.32	-0.38	2.17	0.13	-1.41	Type I
110318A	449542	16.00	16.90	8.00				0.10	-0.48	Type I
110205A	444643	257.00	266.24	3.60	155.40	-7.99	1.94	0.07	-0.77	Type I
110102A	441454	264.00	269.50	8.40	148.55	-2.73	2.12	0.17	-1.15	Type I
101117B	438675	5.20	5.38	4.50	77.00	-0.73	2.17	0.14	-0.52	Type I
101024A	437016	18.70	18.82	5.50	77.02	-0.11	1.82	0.08	-0.95	Type I
101017A	436429	70.00	74.94	9.40	80.98	-2.27	1.90	0.24	-0.65	Type II
100906A	433509	114.40	114.37	10.10	80.24	-3.37	2.03	0.23	-0.95	Type II
100816A	431764	2.90	3.01	10.90	82.85	-1.51	1.91	0.15	-0.29	Type II
100728B	430172	12.10	11.97	3.50	97.05	-1.03	2.04	0.17	-0.58	Type II
100728A	430151	198.50	200.64	5.10	76.72	-0.80	1.90	0.08	-0.54	Type I
100704A	426722	197.50	192.83	4.30		-3.12	2.12	0.16	-1.14	Type I
100621A	425151	63.60	63.62	12.80	76.03	-3.02	2.30	0.07	-0.50	Type I
100619A	424998	97.50	97.86	4.80	76.44	-4.85	2.29	0.20	-0.99	Type I
100615A	424733	39.00	38.85	5.40	62.40	-4.29	2.38	0.09	-0.58	Type I
100522A	422783	35.30	48.00	7.10	65.37	-4.75	2.28	0.13	-1.24	Type I
100119A	383063	23.80	24.38	7.70				0.02	-0.35	Type I
091221	380311	68.50	68.35	3.00	72.37	-1.22	1.71	0.25	-0.66	Type II
091208B	378559	14.90	14.85	15.20	115.14	-0.32	2.03	0.10	-0.97	Type I
091127	377179	7.10	6.98	46.50	3214.62	-1.08	1.80	0.16	-0.63	Type I
091020	373458	34.60	34.94	4.20	81.50	-2.98	2.09	0.20	-0.65	Type II
091018	373172	4.40	4.42	10.30	61.49	-0.41	1.98	0.13	-0.31	Type I
090929B	371050	360.00	362.30	3.30	84.31	-1.02	1.99	0.15	-1.42	Type I
090926B	370791	109.70	101.31	3.20	88.76	-1.01	1.56	0.21	-0.81	Type II
090904B	361831	47.00	64.00	5.30	134.26	0.47	1.81	0.04	-0.62	Type I
090813	359884	7.10	7.23	8.50	78.69	-0.17	1.90	0.17	-0.84	Type I
090812	359711	66.70	72.70	3.60	76.82	-2.32	1.89	0.15	-0.79	Type I

Table 1. (Continued.)

090715B	357512	266.00	266.05	3.80	46.25	-1.13	2.03	0.32	-1.26	Type II
090715A	357498	63.00	62.46	3.90				0.20	-1.79	SGRBwEE
090709A	356890	89.00	88.58	7.80	67.81	-1.87	2.01	0.07	-0.50	Type I
090618	355083	113.20	113.09	38.90	120.90	-5.86	1.92	0.10	-0.54	Type I
090424	350311	48.00	48.90	71.00	84.46	-1.29	1.96	0.41	-1.19	Type II
090401B	348152	183.00	183.30	23.10	73.22	-1.13	1.93	0.39	-1.69	Type II
090301A	344582	41.00	41.09	18.70				0.07	-0.60	Type I
090201	341749	83.00	74.43	14.70	2835.85	-0.66	2.26	0.07	-0.68	Type I
090129	341504	17.50	17.54	3.70				0.18	-0.49	Type II
090102	338895	27.00	27.07	5.50	387.21	-0.50	1.77	0.08	-0.60	Type I
081222	337914	24.00	33.09	7.70	51.75	-2.10	1.99	0.31	-0.69	Type II
081221	337889	34.00	468.93	18.20	68.40	-1.40	2.49	0.44	-1.56	Type II
081203A	336489	294.00	220.03	2.90	83.10	-2.13	2.04	0.27	-1.04	Type II
081126	335647	54.00	58.37	3.70	65.72	-3.01	2.05	0.07	-0.87	Type I
081121	335105	14.00	17.54	4.40	2813.20	-1.45	1.90	0.02	-0.56	Type I
080916A	324895	60.00	56.70	2.70	70.21	-1.32	1.88	0.20	-0.56	Type II
080915B	324805	3.90	3.33	8.50				0.15	-0.37	Type II
080804	319016	34.00	33.66	3.10	99.04	-1.10	1.82	0.21	-0.68	Type II
080727B	318101	8.60	8.58	7.60	101.23	-2.50	1.33	0.09	-0.48	Type I
080721	317508	16.20	92.61	20.90	108.03	-0.63	1.94	0.36	-1.29	Type II
080714	316910	33.00	33.41	4.20	79.71	-1.13	1.69	0.26	-0.80	Type II
080613B	313954	105.00	103.94	2.70	69.46	1.50	2.07	0.26	-0.94	Type II
080607	313417	79.00	79.55	23.10	82.13	-2.35	2.03	0.29	-0.99	Type II
080605	313299	20.00	19.20	19.90	90.39	-0.60	1.75	0.07	-0.54	Type I
080603B	313087	60.00	59.01	3.50	61.77	-3.46	1.83	0.16	-0.96	Type I
080602	312958	74.00	74.30	2.90	111.59	-4.71	1.90	0.13	-1.02	Type I
080515	311658	21.00	20.93	3.90		-0.91	1.77	0.06	-0.63	Type I
080413B	309111	8.00	6.98	18.70	131.25	-0.57	1.93	0.25	-0.56	Type II
080413A	309096	46.00	46.40	5.60	60.67	-2.77	2.15	0.23	-0.88	Type II
080411	309010	56.00	56.38	43.20	70.15	-0.99	1.98	0.06	-0.88	Type I
080409	308812	20.20	22.72	3.70	84.03	-0.71	2.07	0.17	-1.16	Type I
080328	307931	90.60	90.88	5.50	99.44	-7.70	1.95	0.13	-0.80	Type I
080319C	306778	34.00	29.95	5.20	223.69	1.50	1.61	0.28	-0.72	Type II
080229A	304379	64.00	64.00	5.70	90.34	-3.71	1.81	0.21	-0.93	Type II
080218B	303631	6.20	6.21	3.10	930.98	-1.04	2.30	0.11	-0.67	Type I
071117	296805	6.60	6.34	11.30	2848.00	-0.89	2.05	0.24	-0.52	Type II
071020	294835	4.20	4.48	8.40	61.24	-0.66	1.60	0.10	-0.31	Type I

Table 1. (Continued.)

071003	292934	150.00	148.29	6.30		-0.51	1.91	0.34	-1.22	Type II
070917	291292	7.30	8.77	8.50		-0.90	1.12	0.26	-0.58	Type II
070911	290624	162.00	161.54	3.90		-1.57	2.03	0.06	-0.73	Type I
070714B	284856	64.00	63.94	2.70	61.37	-1.63	2.07	0.26	-1.75	SGRBwEE
070628	283320	39.10	39.10	5.10	110.82	-0.68	2.04	0.25	-0.74	Type II
070521	279935	37.90	38.27	6.53	76.89	-0.13	2.00	0.12	-0.62	Type I
070508	278854	20.90	21.06	24.10	75.92	-0.26	1.83	0.06	-0.48	Type I
070420	276321	76.50	76.48	7.12	100.68	-4.45	1.98	0.13	-0.70	Type I
070328	272773	75.30	63.49	4.22	88.29	-1.34	2.14	0.23	-0.54	Type II
070306	263361	209.50	208.96	4.07	153.20	-3.21	1.94	0.21	-1.18	Type I
070220	261299	129.00	136.70	5.88	78.79	-1.27	1.55	0.28	-0.92	Type II
061222A	252588	71.40	96.00	8.53	101.02	-4.29	1.93	0.25	-1.18	Type II
061210	243690	85.30	85.25	5.31		-1.71	2.86	0.09	-2.41	SGRBwEE
061126	240766	70.80	202.18	9.76	1599.69	-1.34	1.92	0.38	-1.49	Type II
061121	239899	81.30	81.41	21.10	55.40	-3.88	1.90	0.29	-1.14	Type II
061021	234905	46.20	46.53	6.11	72.79	-2.01	1.99	0.31	-1.02	Type II
061007	232683	75.30	74.69	14.60	80.45	-1.95	2.00	0.09	-0.52	Type I
061006	232585	129.90	129.92	5.24	156.58	-0.78	1.87	0.23	-1.98	SGRBwEE
060927	231362	22.50	22.59	2.70	64.72	-0.73	1.95	0.18	-0.72	Type II
060912A	229185	5.00	5.06	8.58	108.88	-1.07	1.89	0.20	-0.47	Type II
060908	228581	19.30	19.33	3.03	71.68	-0.53	2.13	0.09	-0.47	Type I
060904A	227996	80.10	80.13	4.87	65.96	-3.56	1.25	0.12	-0.74	Type I
060825	226382	8.00	8.00	2.66	65.59	-1.04	1.76	0.03	-0.30	Type I
060814	224552	145.30	144.32	7.27	71.54	-1.96	2.12	0.18	-0.82	Type I
060813	224364	16.10	16.06	8.84	76.24	-0.28	1.92	0.22	-0.46	Type II
060614	214805	108.70	109.25	11.50	91.40	1.50	1.90	0.10	-0.92	Type I
060510A	209351	20.40	20.29	14.70	146.15	-2.29	1.89	0.12	-0.68	Type I
060421	206257	12.20	11.46	2.94	87.56	-1.10	1.55	0.09	-0.48	Type I
060418	205851	103.10	144.00	6.52	77.97	-1.54	1.94	0.15	-1.11	Type I
060306	200638	61.20	60.99	5.97	87.52	-3.92	2.29	0.17	-1.32	Type I
060223B	192152	10.30	10.37	2.87	68745.00		2.00	0.06	-0.39	Type I
060210	180977	255.00	288.00	2.72	94.95	-1.26	2.08	0.16	-1.22	Type I
060206	180455	7.60	7.55	2.79	58.35	-0.81	2.20	0.13	-0.38	Type I
060117	177666	16.90	16.90	48.30				0.08	-0.67	Type I
060105	175942	54.40	53.82	7.44	86.89	-1.13	2.05	0.13	-0.52	Type I
051111	163438	46.10	64.00	2.66		-1.60	2.23	0.19	-0.75	Type II
051109A	163136	37.20	37.25	3.94	119.66	-3.13	2.07	0.20	-0.99	Type I

Table 1. (Continued.)

050922C	156467	4.50	4.54	7.26		-1.05	2.21	0.08	-0.41	Type I
050820B	151334	12.00	12.22	3.95		-1.77	1.98	0.11	-0.40	Type I
050802	148646	19.00	19.01	2.75		1.09	1.86	0.13	-0.58	Type I
050724	147478	96.00	96.58	3.26		-0.01	1.80	0.10	-1.83	SGRBwEE
050717	146372	85.00	85.06	6.23		-1.95	1.79	0.26	-1.05	Type II
050713A	145675	124.70	124.67	4.67		-5.65	2.20	0.17	-1.09	Type I
050701	143708	21.80	21.57	2.74		-1.19	2.33	0.11	-0.72	Type I
050603	131560	12.40	21.06	21.50		-1.71	2.02	0.15	-1.19	Type I
050525A	130088	8.80	8.83	41.70		-0.68	2.09	0.05	-0.42	Type I
050418	114893	82.30	82.30	3.68				0.11	-0.85	Type I
050416B	114797	3.40	4.03	5.93	310326.00			0.08	-0.51	Type I
050416A	114753	2.50	2.50	4.88		-0.70	2.06	0.12	-0.51	Type I
050401	113120	33.30	32.13	10.70		-0.58	1.79	0.12	-0.83	Type I
050326	112453	29.30	29.31	12.20		-1.69	2.04	0.06	-0.70	Type I
050318	111529	32.00	16.13	3.16		-1.12	1.98	0.33	-1.35	Type II
050306	107547	158.30	159.81	3.58	127308.00			0.07	-0.83	Type I
050219B	106442	30.70	28.93	24.80		-1.23	2.18	0.14	-0.76	Type I
050219A	106415	23.70	23.81	3.53		-2.96	1.58	0.05	-0.42	Type I
050128	103906	19.20	28.03	7.42		-0.95	1.99	0.18	-0.84	Type I
050124	103647	4.00	4.03	5.46		-1.63	1.97	0.06	-0.43	Type I
041224	100703	177.20	178.11	2.94				0.11	-0.85	Type I
041223	100585	109.10	109.12	7.35		-1.88	2.13	0.19	-0.76	Type II

* in the unit of seconds

† in the unit of photons $\text{cm}^{-2} \text{s}^{-1}$

3. Prompt Emission Properties

In this section, we search subgroups in LGRBs by applying a cluster analysis based on the Gaussian mixture model to the dataset of LGRBs each of which is composed of a pair of the two quantities $ADCL$ and \bar{C}/C_{\max} introduced in the previous section.

The `Mclust` package (Fraley & Raftery 2002; Fraley et al. 2012) in the R language is used to select the optimal model via the EM algorithm. First, we apply the method to the one dimensional distributions of LGRBs with respect to $ADCL$ and \bar{C}/C_{\max} separately and find how many components are needed to describe each distribution. Then we apply the same method to the two dimensional distribution of LGRBs. The number of components is optimized according to the Bayesian information criterion (BIC). Details of the Gaussian mixture model, the EM algorithm, and BIC are described in Appendix 1.

3.1. One-dimensional cluster analysis

The left and right panels of Figure 2 show the histograms of $ADCL$ and $\log(\bar{C}/C_{\max})$, respectively. The ordinate of each panel represents the frequency density with respect to the parameter. Note that the total area of the shaded region is equal to unity. From these $ADCL$ and $\log(\bar{C}/C_{\max})$ distributions, we estimate the optimal probability densities based on the Gaussian mixture model (see Appendix 1 for details). In Tables 2 and 3, we list the number of components, the logarithm of the likelihood function, and the BIC for the optimal models. The tables indicate that two component models are best fitted to both of the $ADCL$ and $\log(\bar{C}/C_{\max})$ distributions. The solid lines in Figures 2 indicate the optimal density profiles of the two-component Gaussian mixture model.

Table 2. Number of components $\#$, the logarithm of the likelihood function, and BIC for optimal Gaussian mixture model on the $ADCL$ distribution.

$\#$	$\log(\text{likelihood})$	BIC
1	151.2	292.2
2	169.9	314.1
3	174.0	307.0

Table 3. Number of components $\#$, logarithm of likelihood function, and BIC of Gaussian mixture model on $\log(\bar{C}/C_{\max})$ distribution.

$\#$	$\log(\text{likelihood})$	BIC
1	-81.8	-173.8
2	-62.9	-146.3
3	-53.4	-147.8

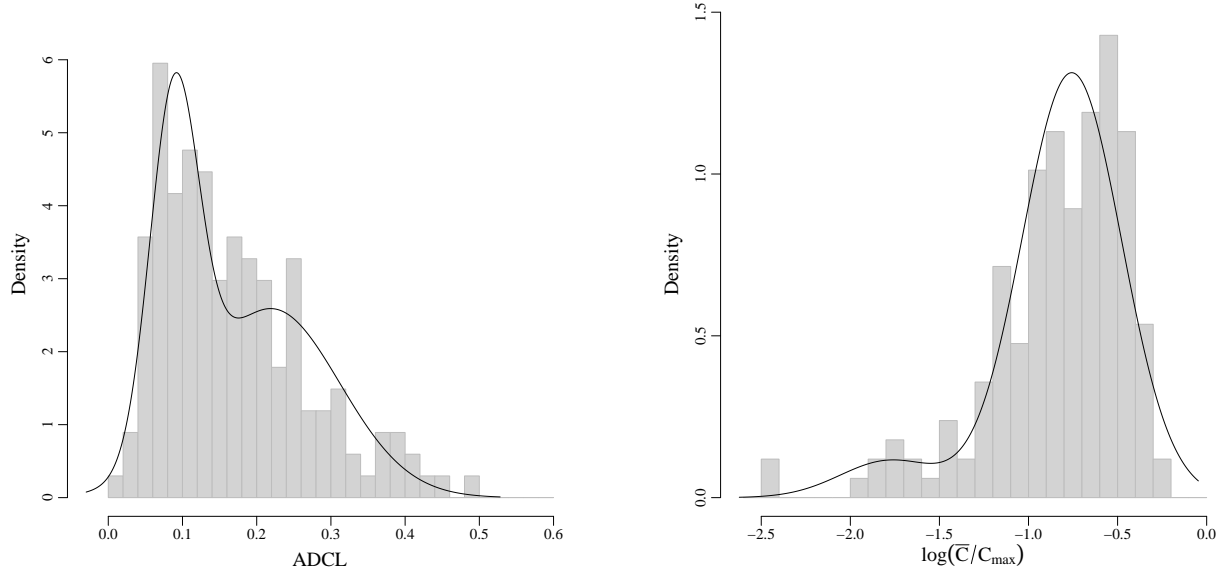


Fig. 2. The histograms of $ADCL$ (left) and $\log(\bar{C}/C_{\max})$ (right), respectively. The vertical axes show not frequency but frequency density. The solid lines indicates the optimal models with two component Gaussian mixture model.

3.2. Two-dimensional cluster analysis

Next we apply the cluster analysis to the two-dimensional distribution in the $ADCL - \log(\bar{C}/C_{\max})$ diagram. In Table 4, we list the number of components, the logarithm of the likelihood function, and BIC for the optimal models. Figure 3 shows the distribution of LGRBs in the two-dimensional space of $ADCL$ and $\log(\bar{C}/C_{\max})$. The result of the cluster analysis with three components is shown as coloring of symbols. The red asterisks denote Type I LGRBs and the blue crosses Type II LGRBs, following the definition by Tsutsui et al. (2013). The green circles denote contaminating SGRBwEE. The solid ellipses in Figure 3 indicate the optimal density profiles of each Gaussian component. The optimal mixing probability π , mean vector μ , and variance matrix σ for each component are listed in Table 5.

Table 4 indicates that the four-component model which divides Type I LGRBs into two subclasses fits the data best, but the difference of BIC between four-component model and three-component model is quite small. Furthermore, GRBs belonging to the two subclasses in Type I LGRBs exhibit similar light curves of the X-ray afterglow, which are clearly distinct from those of Type II LGRBs (See Appendix 2 for the results of four-component model analysis). Then as a tentative model, we adopt three-component model in the following to simplify the argument. To determine the true number of groups, we need a larger number of sample with more accurate estimation of parameters. Therefore we will leave it as a subject in future works.

We show all of light curves classified into each subclass in Figures 8 - 16. Each light curve is constructed with 100 bins to reduce noise, although we use 64 ms bin light curves to

calculate $ADCL$ and $\log(\bar{C}/C_{\max})$. These figures show that the pulses in a Type II LGRB progressively decline, while each pulse in a Type I LGRB emits a similar amount of energy. Because the pulse is thought to be caused by the collision of shells, the pulse shape may be used to probe the formation mechanism of shells and thus the energy injection from the central engine. Therefore the decline of pulse heights in a Type II LGRB indicates that the energy injected by central engine decreases. On the other hand, the central engine of a Type I LGRB seems to maintain the energy injection rate during the prompt emission. We will discuss the origin of the difference after looking at properties of X-ray afterglow emission of these two types of LGRBs.

Table 4. Number of components $\#$, logarithm of likelihood function, and BIC of Gaussian mixture model on $ADCL$ and logarithm \bar{C}/C_{\max} distribution.

$\#$	$\log(\text{likelihood})$	BIC
1	91.6	157.5
2	133.7	221.3
3	154.4	242.1
4	173.8	245.2
5	171.5	235.4

Table 5. The mixing probability π , mean vector μ , and variance matrix σ for each component of the three-components Gaussian mixture model.

	Type I LGRB	Type II LGRB	SGRBwEE
π	0.61	0.35	0.042
μ	(0.11, -0.72)	(0.27, -0.90)	(0.17, -1.99)
σ	$\begin{pmatrix} 0.0027 & -0.0097 \\ -0.0097 & 0.090 \end{pmatrix}$	$\begin{pmatrix} 0.0052 & -0.018 \\ -0.018 & 0.088 \end{pmatrix}$	$\begin{pmatrix} 0.0071 & 0.022 \\ 0.022 & 0.086 \end{pmatrix}$

4. X-ray Afterglow Properties

Contrary to expectations before the launch of *Swift*, the majority of early X-ray afterglows observed by *Swift* show a complex time profile called the 'canonical' light curve which consists of three segments with power-law decays : the first steep decay phase with the decay index $\alpha \sim -3 - -5$, the second shallow phase with $\alpha \sim -0.5$, and the third normal phase with $\alpha \sim -1.3$ (Nousek et al. 2006; Zhang et al. 2006). They sometimes have the fourth phase called the post jet break phase with $\alpha \sim -2$.

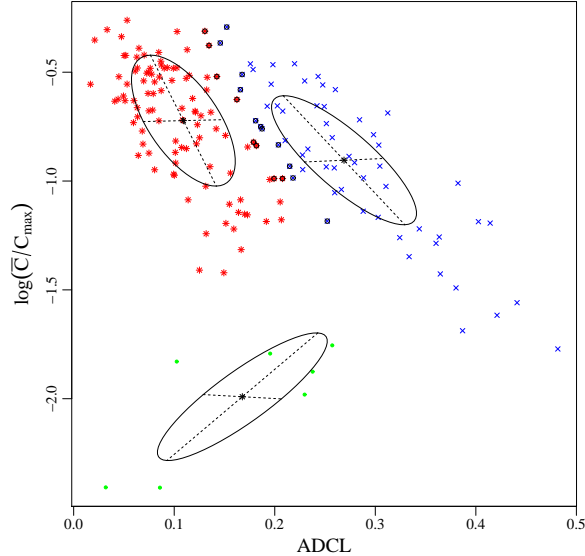


Fig. 3. The relationship between $ADCL$ and $\log(\bar{C}/C_{\max})$ with the result of the clustering analysis based on three-components Gaussian mixture model. The result of cluster analysis is shown as the coloring of symbols. The red asterisks are referred as Type I LGRBs, the blue crosses as Type II LGRBs, and the green circles as SGRBwEE. The optimal Gaussian distributions are indicated by ellipses. The symbols marked with circles show the events whose uncertainty of classification are larger than 0.2 and removed from following afterglow analysis (See section 4.).

In addition to the complexity, what makes the variation of X-ray afterglow light curves is an issue of wide interest in the GRB study. According to Evans et al. (2009), 4 % of GRBs have no break in their X-ray afterglows, 30 % one break (with flattening or steepening), and the rest at least two breaks. The last group was divided into 'canonical' (42 %) and 'oddball' (24 %) : if an X-ray afterglow light curve contains a flattening break with $\Delta\alpha \geq 0.5$ followed by a steepening break with $\Delta\alpha \leq -0.5$, it is regarded as canonical, and otherwise oddball.

Willingale et al. (2007) first showed that X-ray afterglow light curves can be fitted using two components with an early exponential decay phase followed by a power-law decay. Other authors (Ghisellini et al. 2009; Yamazaki 2009) showed that the two components are sufficient to explain the complexity and variation in the afterglow emission. On the other hand, what makes the second component and determines the ratio of energies injected to these components remains unresolved. In the previous section, we have developed a new classification scheme of LGRBs based on the light curve properties exclusively of the prompt emission. The different subclasses thus introduced are expected to have different progenitors or central engines. Therefore it is natural to think that there are also some differences in properties of their afterglow emission.

Figure 3 shows that there are some LGRBs around the border line on which the conditional probability of Type I is equal to that of Type II. The probability of classification errors is not negligible around the line, and misclassifications can disturb the following analysis. We

thereby remove events whose uncertainties of classification are greater than 0.2 from the following analysis. In Figure 3, we marked such 19 events with circles. In addition, we found 7 Type II LGRBs with weak precursors (120802A, 120326A, 091221, 080229A, 070628, 061222A, 061121). Although our classification method does not distinguish them from the other Type II events, there is a clear difference in the shapes of their cumulative light curves. Cumulative light curves of these 7 events exhibit shapes of convex functions of time while the other Type II events have the cumulative light curves with concave shapes (see Figs. 13 - 14). Therefore we exclude this small number of events in the following analyses. Furthermore, we do not consider SGRBwEE because of the small number of the sample.

In Figures 4 and 5, we show the histograms of α_{init} and β_{XRT} , respectively. The figures obviously indicate that Type I and Type II LGRBs have different XRT initial temporal and spectral indices in their X-ray afterglow emission. Two-sample Kolmogorov-Smirnov (KS) test shows $p = 0.082$ for α_{init} , and $p = 0.070$ for β_{XRT} , respectively. These large values might be due to a feature of KS test, i.e., the p-value is more sensitive to the median values of the distributions than the long tails that we would like to focus. If we use only the LGRBs whose α_{init} less than -2, the vertical line in Figure 4, KS test shows $p = 0.0039$. This p -value indicates the difference is significant at nearly $3\text{-}\sigma$ confidence level. To examine the temporal index in the steep decay phase, we need to know the starting time of XRT observations because the steep decay phase might be missed if the XRT starts observation too late. Figure 6 shows the relationship between $\log(T_{\text{start}}^{\text{XRT}}/T_{90})$ and α_{init} for Type I (left) and Type II (right) LGRBs, respectively. If LGRBs do not have steep decay or XRT observations started after steep decay phase, these points distribute in a cluster whose α_{init} is in excess -2. We therefore roughly estimate that the indices for Type I LGRBs distribute between -6 and -3 while those for Type II LGRBs between -3 and -2. We will make a more thorough discussion after the analysis of XRT light curve shape (Tsutsui & Shigeyama in prep).

5. Implications for central engines

There are two prominent theoretical candidates for the central engine of LGRBs: a black hole with an accretion disk (Woosley 1993), hereafter the collapsar model, and a strongly magnetized proto neutron star (Usov 1992; Duncan & Thompson 1992), the magnetar model. Though these two models have been vigorously studied by many authors (MacFadyen & Woosley 1999; Proga & Begelman 2003; Bucciantini et al. 2008; Bucciantini et al. 2009; Nagataki 2011; Metzger et al. 2011), which engine is really responsible for LGRBs is still controversy. In this section, we briefly discuss how we can connect our classification with these two different central engine models.

The features of Type I and Type II LGRBs are summarized as below:

- The prompt emission of Type I LGRBs consists of several separated pulses with similar

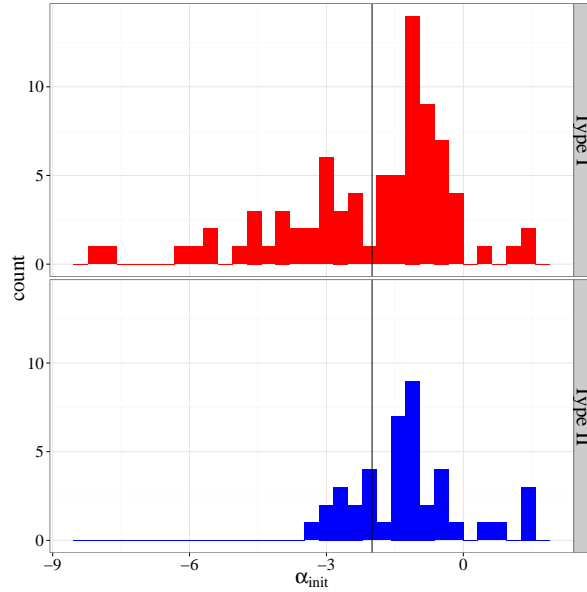


Fig. 4. The histograms of α_{init} for Type I (top) and Type II (bottom) LGRBs, respectively.

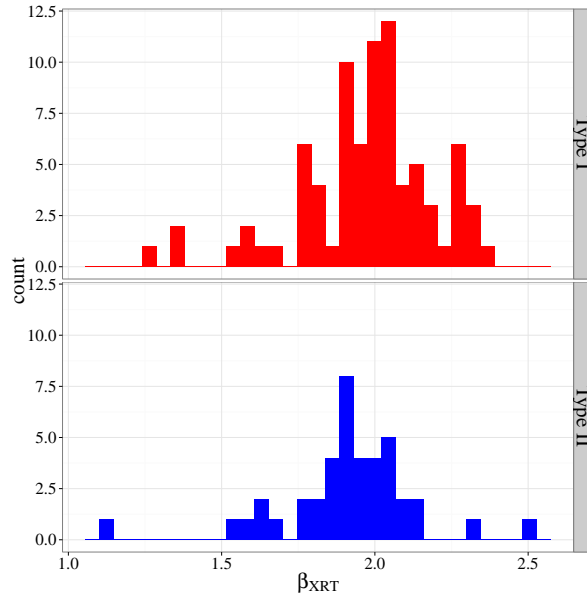


Fig. 5. The histograms of β_{XRT} for Type I (top) and Type II (bottom) LGRBs, respectively.

heights and sharply decreases with decay index between -3 and -6 .

- The prompt emission of Type II LGRBs has a broad peak and slowly decreases with index between -2 and -3 .

These light curves imply that the central engine of Type I LGRBs injects energies by several violent episodes with similar scales. An accreting black hole potentially makes such episodes because the accretion disk is formed only when the specific angular momentum of the stat

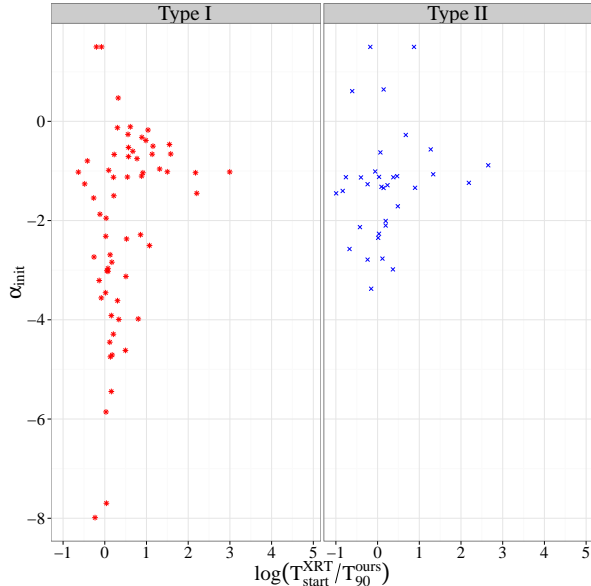


Fig. 6. The relationship between $\log(T_{\text{start}}^{\text{XRT}}/T_{90}^{\text{ours}})$ and α_{init}

exceeds the critical value. López-Cámara et al. (2010) showed that the radial distribution of the specific angular momentum in the star can be reflected in the variability and quiescent time in LGRBs.

On the other hand, the central engine of a Type II LGRBs continuously inject energies by a single major event decaying inversely proportional to the square of time. From these light curve properties of Type II LGRBs, we suggest that magnetic dipole radiation from a proto-magnetar may be responsible for the decay part of their prompt emission.

6. Summary and Discussion

Using the complete sample of the bright *Swift* LGRBs, we have confirmed the subclasses in LGRBs first discovered by Tsutsui et al. (2013). We use parameters characterizing light curve shapes to avoid influence of nuisance parameters such as the distance and jet opening angle. We do not use the duration, hardness ratio or fluence depending on nuisance parameters.

We should notify the readers that our classification method is not exactly the same with our previous works (Tsutsui et al. 2013; Tsutsui & Shigeyama 2013). Although there are some fraction of LGRBs referred to as 'outlier' from the fundamental planes, which probably belong to unclassified types of LGRBs, we can not consider them in this paper because of the lack of the redshifts and prompt spectral parameters. To study statistical properties of Type I and Type II LGRBs more accurately, we need to somehow detect contamination of our sample by outliers and remove them from the analysis. In Tsutsui & Shigeyama (2013), we found that Type I and Type II LGRBs show a canonical X-ray afterglow, while outliers do not. If we use the light-curve shape of X-ray afterglow instead of the fundamental planes, it seems to be

possible to detect outliers contaminating Type I and II GRBs classified in this paper. and it enables us to identify more accurate properties of X-ray afterglow of these subclasses. The analysis of X-ray afterglows, however, is beyond the scope of this paper, therefore we have roughly discussed only the difference in the X-ray afterglows. A more detailed statistical study of the parameters of canonical light curves for Type I and Type II LGRBs is a subject in our future work (Tsutsui and Shigeyama in prep).

Before we summarize this paper, we need to stress the importance of the study of systematic errors in observations. We use light curves in the fixed *Swift* 150-350 keV energy band, which means that we use different energy bands in the rest frames of different GRBs. From this viewpoint, the bolometric flux light curve seems to be more appropriate to discuss the subclasses of LGRBs. Though broad band observations are inevitable to determine the spectral shape of the prompt emission, the band width of BAT detector onboard *Swift* is too narrow to do so. The future Chinese-French mission *SVOM* will provide a good opportunity to construct bolometric light curves by broader band observations with ECLAIR and GRM and to confirm or falsify our present classifications.

With the result of our previous paper (Tsutsui et al. 2013), LGRBs are divided into three subgroups as follows:

- Type I LGRBs exhibiting linearly increasing cumulative light curves of the prompt emission reside on a fundamental plane and show canonical light curves in their X-ray afterglow. The central engine of this type of LGRBs seem to originate from an accretion disk around a black hole.
- Type II LGRBs with long tailed prompt emission reside on the other fundamental plane and show canonical light curve in their X-ray afterglow with a steep decay phase slower than Type I and seem to originate from a magnetar.
- outliers which do not reside on either of the fundamental planes and do not show a canonical light curve.

Type I and Type II LGRBs on the separate fundamental planes can be used as distance indicators like other empirical correlations of GRBs (Liang & Zhang 2005; Ghirlanda et al. 2006; Schaefer 2007; Kodama et al. 2008; Liang et al. 2008; Amati et al. 2008; Cardone et al. 2009; Tsutsui et al. 2009). They are so tight that they provide much more accurate distance measurements than previous studies (Tsutsui et al. 2012).

Acknowledgments

This work made use of data supplied by the UK Swift Science Data Centre at the University of Leicester. This work is supported in part by the Grant-in-Aid for Young Scientists (B) from the Japan Society for Promotion of Science (JSPS), No.24740116(RT).

Appendix 1. Statistical method

We briefly explain the statistical method used in the section 3. We explain the Gaussian mixture model and the EM algorithm to select optimal parameters with a fixed number of clusters first and then explain the Bayesian Information Criterion (BIC) to select the optimal number of clusters. For details of the statistical method, we refer the reader to an excellent text book Bishop 2006 (Chapter 9 for Gaussian mixture model and EM algorithm and Chapter 4 for BIC).

A.1.1. Gaussian mixture model and EM algorithm

Let us start with an assumption that a data vector comes from a Gaussian mixture model with the density

$$p(\mathbf{x}) = \sum_{k=1}^G \pi_k \mathcal{N}(\mathbf{x} | \boldsymbol{\mu}_k, \boldsymbol{\Sigma}_k), \quad (\text{A1})$$

where \mathbf{x} is a D -dimensional data vector, G is the number of clusters, π_k is a mixing probability of a data element \mathbf{x} belonging to the k th component, and $\mathcal{N}(\mathbf{x} | \boldsymbol{\mu}_k, \boldsymbol{\Sigma}_k)$ is a D -dimensional Gaussian density of the k component given by

$$\mathcal{N}(\mathbf{x} | \boldsymbol{\mu}_k, \boldsymbol{\Sigma}_k) = \frac{\exp\left\{-\frac{1}{2}(\mathbf{x} - \boldsymbol{\mu}_k)^T \boldsymbol{\Sigma}_k^{-1} (\mathbf{x} - \boldsymbol{\mu}_k)\right\}}{(2\pi)^{D/2} |\boldsymbol{\Sigma}_k|^{1/2}} \quad (\text{A2})$$

where $\boldsymbol{\mu}_k$ and $\boldsymbol{\Sigma}_k$ are the mean vector and the variance matrix for the k th component, respectively. The mixing probability must satisfy the constraint that $\sum_{k=1}^G \pi_k = 1$, and $\pi_k \geq 0$.

Given a sequence of independent data $X = \{\mathbf{x}_1, \mathbf{x}_2, \dots, \mathbf{x}_N\}$, we want to maximize the following log-likelihood function

$$\ln p(\mathbf{X} | \boldsymbol{\pi}, \boldsymbol{\mu}, \boldsymbol{\Sigma}) = \sum_{i=1}^N \ln \left\{ \sum_{k=1}^G \pi_k \mathcal{N}(\mathbf{x}_i | \boldsymbol{\mu}_k, \boldsymbol{\Sigma}_k) \right\}. \quad (\text{A3})$$

Taking a derivative of equation (A3) with respect to $\boldsymbol{\mu}_k$ and equating it to 0, we obtain the following equation

$$\boldsymbol{\mu}_k = \frac{1}{N_k} \sum_{i=1}^N \gamma_{ik} \mathbf{x}_i, \quad (\text{A4})$$

where γ_{ik} is called the responsibility and given by the following equation,

$$\gamma_{ik} = \frac{\pi_k \mathcal{N}(\mathbf{x}_i | \boldsymbol{\mu}_k, \boldsymbol{\Sigma}_k)}{\sum_{j=1}^G \pi_j \mathcal{N}(\mathbf{x}_i | \boldsymbol{\mu}_j, \boldsymbol{\Sigma}_j)}, \quad (\text{A5})$$

and

$$N_k = \sum_{i=1}^N \gamma_{ik}. \quad (\text{A6})$$

Similarly, we can obtain the form of the variance matrix by taking the derivative of equation (A3) with respect to $\boldsymbol{\Sigma}_k$ and equating it to 0,

$$\boldsymbol{\Sigma}_k = \frac{1}{N_k} \sum_{i=1}^N \gamma_{ik} (\mathbf{x}_i - \boldsymbol{\mu}_k)(\mathbf{x}_i - \boldsymbol{\mu}_k)^T. \quad (\text{A7})$$

To obtain the form of the mixing probability π_k , we must take into account the constraint that $\sum \pi_k = 1$. Using the Lagrange multiplier method, we obtain the following equation

$$\pi_k = \frac{N_k}{N}. \quad (\text{A8})$$

Because γ_{ik} itself is a function of the model parameters, equations (A4), (A7), (A8) do not give solutions. To obtain optimal solutions for these parameters, we need to follow an iterative procedure called the EM algorithm as below:

1. Setting initial guesses for $\boldsymbol{\mu}_k$, $\boldsymbol{\Sigma}_k$, and π_k and calculate the initial value of the log-likelihood function.
2. Using the current value of parameters, calculate the responsibility γ_{ik} from equation (A5). (E step)
3. Using the current value of the responsibility γ_{ik} , calculate parameters from equations (A4), (A7), (A8). (M step)
4. Calculate the log-likelihood function, and check the convergence of the parameters or log-likelihood. If convergence criteria are not satisfied, return to step 2.

Given the optimal Gaussian mixture model density and a data vector \mathbf{x} , the class K and the uncertainty of classification p_{mis} of the data are determined by,

$$K = \text{which.max}_k[\pi_k \mathcal{N}(\mathbf{x} | \boldsymbol{\mu}_k, \boldsymbol{\Sigma}_k)], \quad (\text{A9})$$

and

$$p_{\text{mis}} = 1 - \pi_K \mathcal{N}(\mathbf{x} | \boldsymbol{\mu}_K, \boldsymbol{\Sigma}_K), \quad (\text{A10})$$

respectively. Here $\text{which.max}_k[X_k]$ is a function that returns the value of the index k yielding the maximum value of X_k .

A.1.2. Bayesian Information Criterion BIC

To select the optimal number of clusters, `mclust` package uses the Bayesian Informative Criterion (*BIC*)

$$BIC = 2 \ln p_{\mathcal{M}}(\mathbf{x} | \boldsymbol{\pi}^*, \boldsymbol{\mu}^*, \boldsymbol{\Sigma}^*) - N_p \ln(N), \quad (\text{A11})$$

where $\ln p_{\mathcal{M}}(\mathbf{x} | \boldsymbol{\pi}^*, \boldsymbol{\mu}^*, \boldsymbol{\Sigma}^*)$ is the maximized log-likelihood function for the model and data, N_p is the number of independent parameters for the model \mathcal{M} . The log-likelihood increases with increasing number of the model parameters and is likely to result in overfitting. The BIC selects the optimal number of clusters by giving a penalty for adding parameters.

Appendix 2. Four component model

In this section, we show the results when we assume four-component model in the $ADCL - \log(\bar{C}/C_{\max})$ diagram. The upper left panel of Figure 7 shows the four-component model divides Type I LGRBs into two subclasses (red asterisks and orange triangles). However, the other panels indicate that X-ray afterglow properties of these two subclasses are hardly distinguishable. This is why we adopted three-component model in the main discussion.

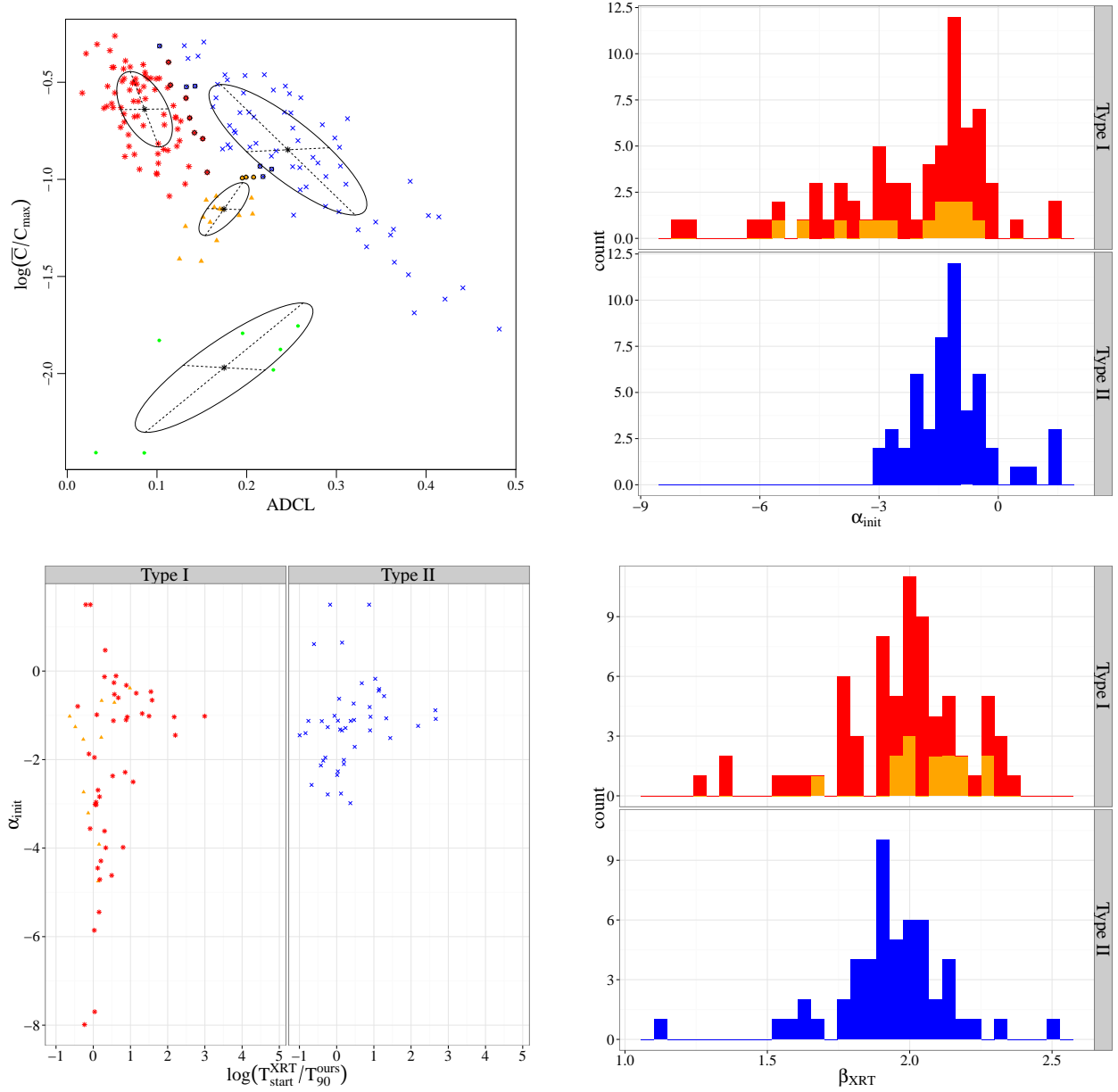
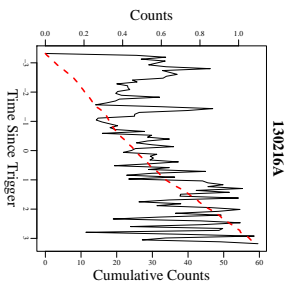
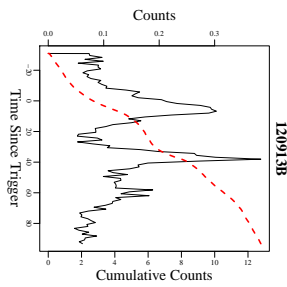
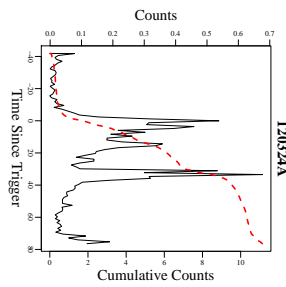
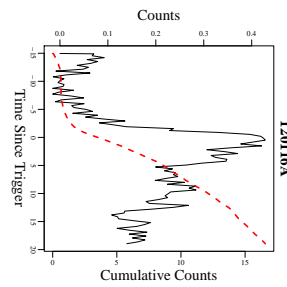
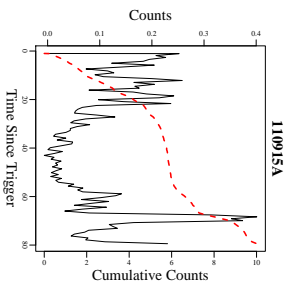
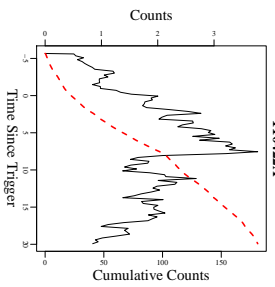
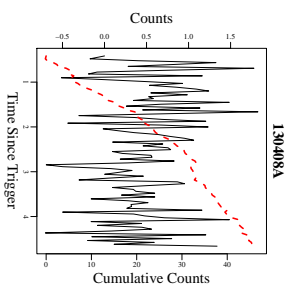
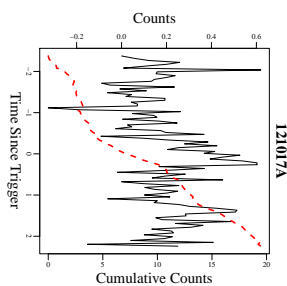
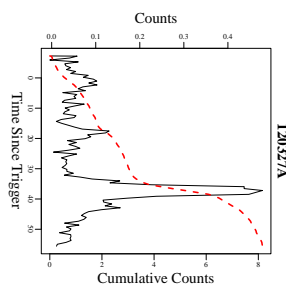
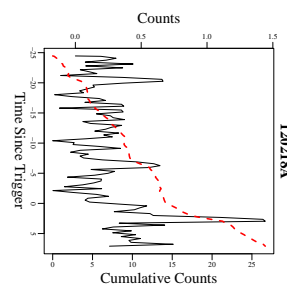
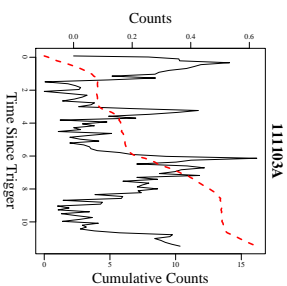
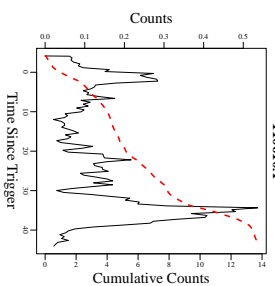
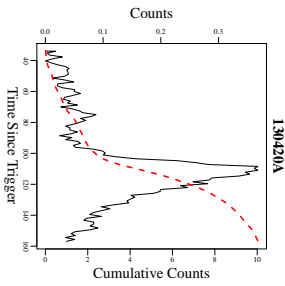
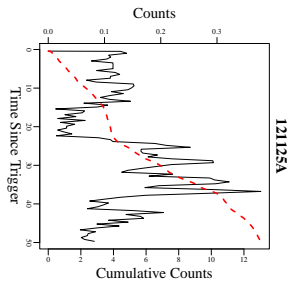
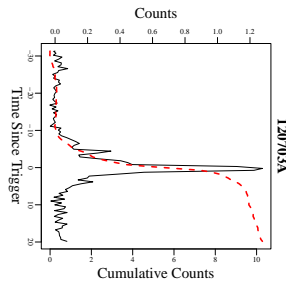
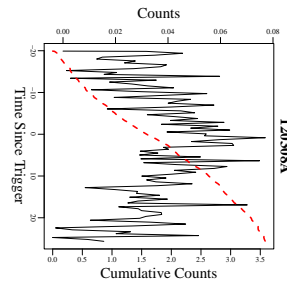
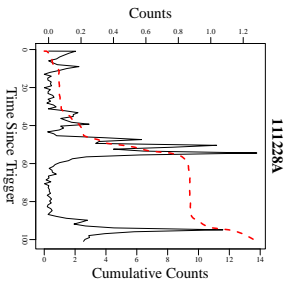
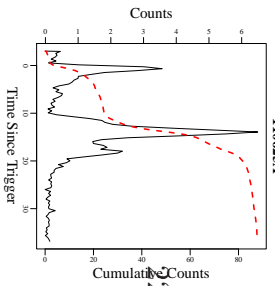
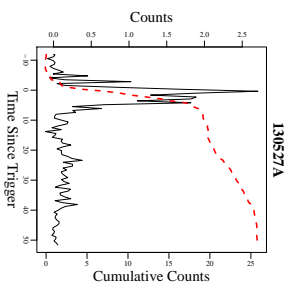
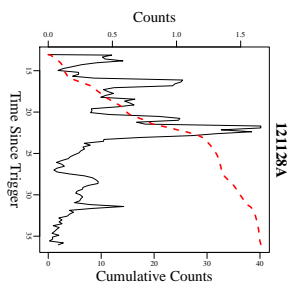
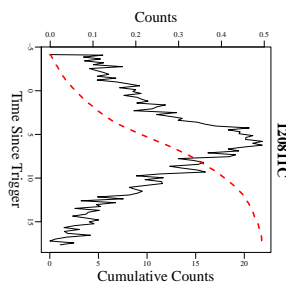
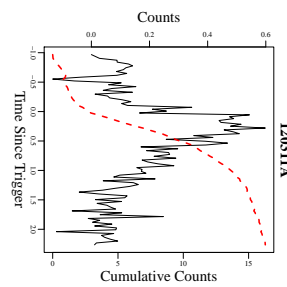
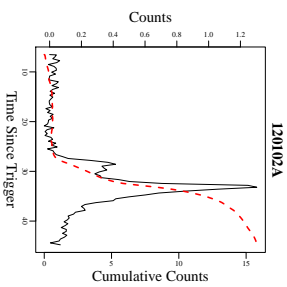
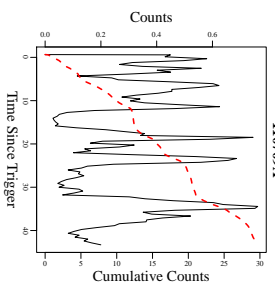


Fig. 7. The same figures as Figure 3 – 6, but we assumed four-component model in the $ADCL - \log(\bar{C}/C_{\max})$ diagram.



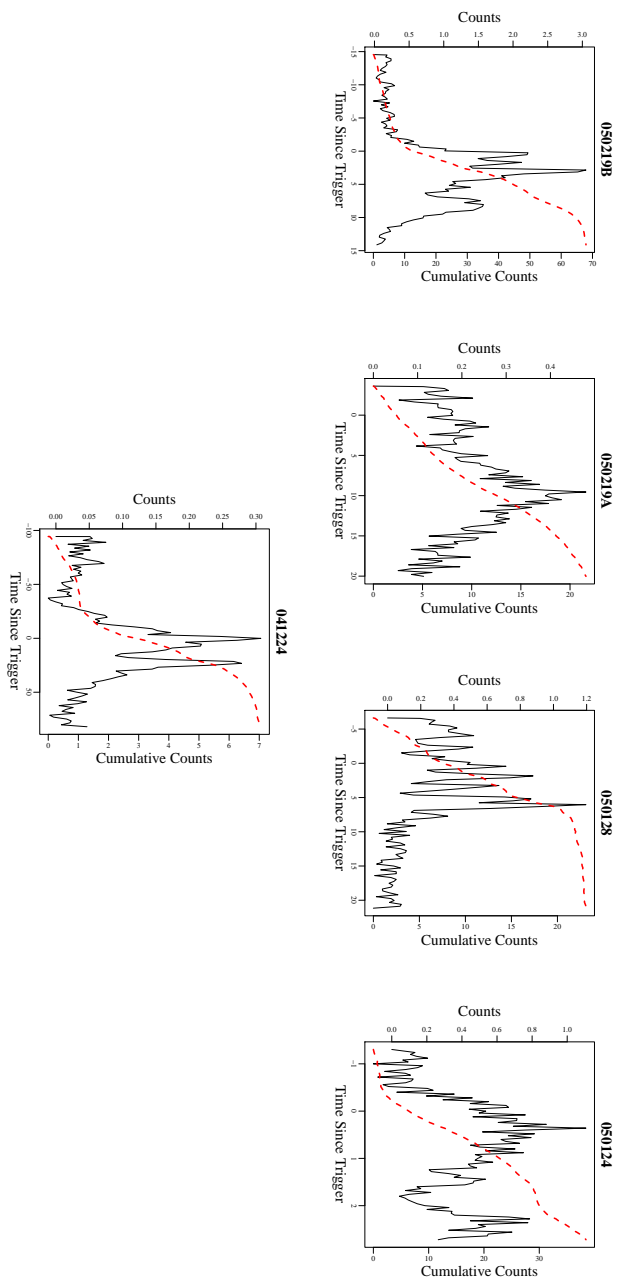


Fig. 12. Light curves (black solid) and cumulative light curves (red dotted) of Type I LGRBs.

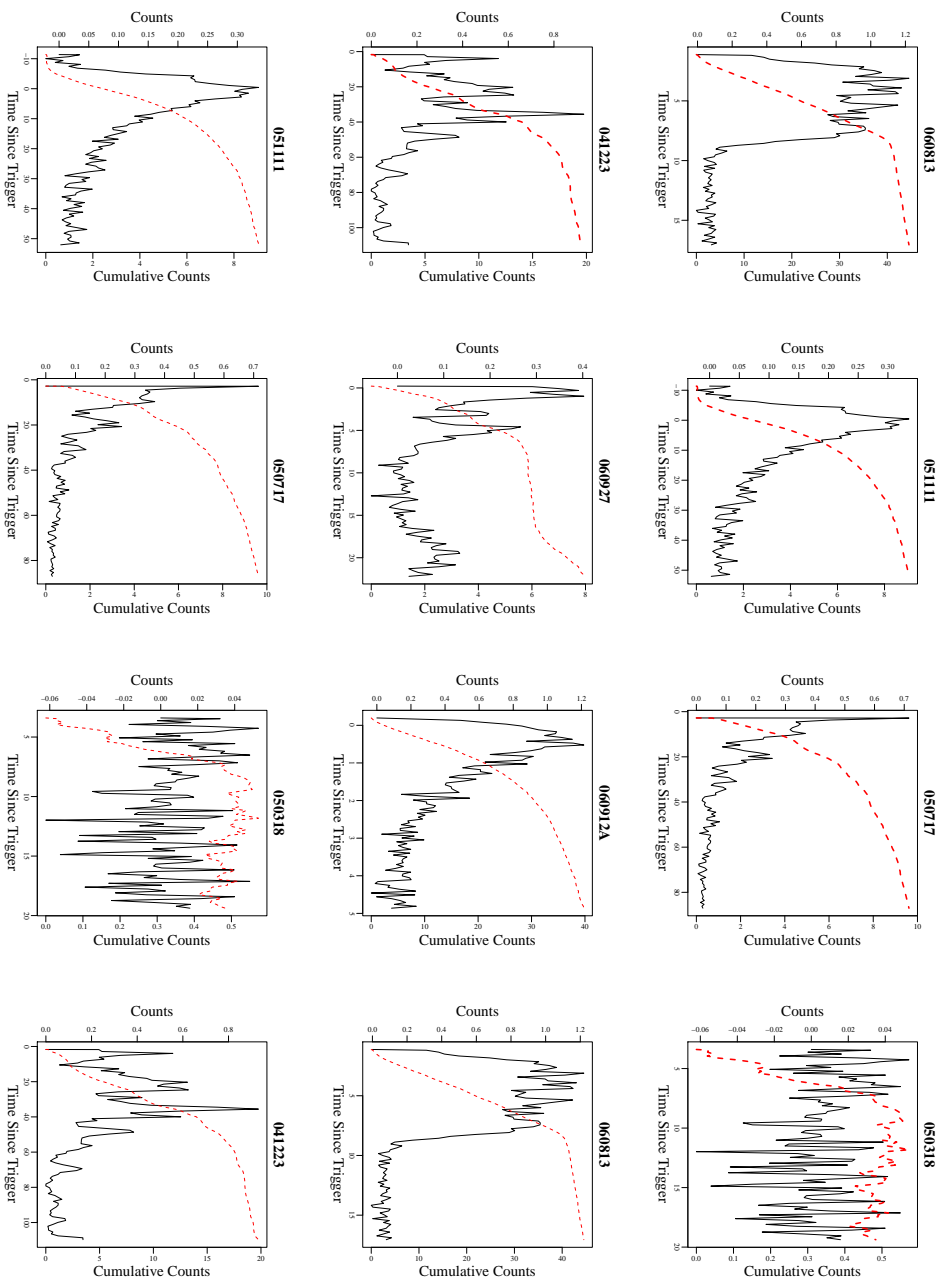


Fig. 15. Light curves (black solid) and cumulative light curves (red dotted) of Type II LGRBs.

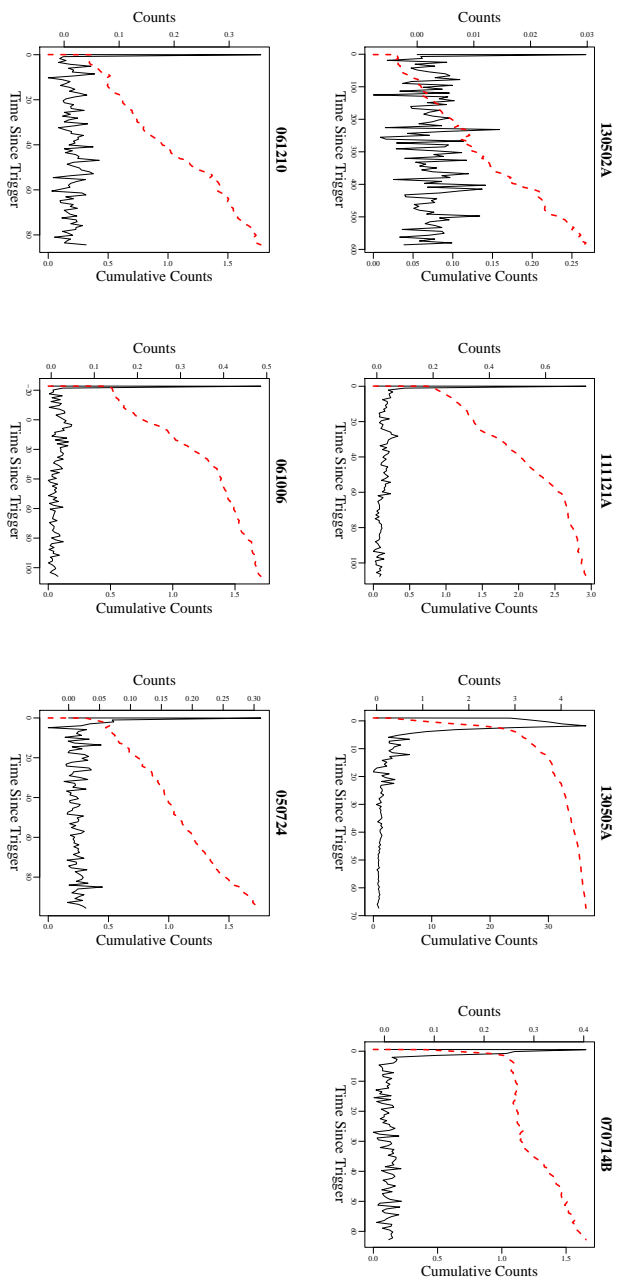


Fig. 16. Light curves (black solid) and cumulative light curves (red dotted) of SGRBwEE.

References

- Amati, L., Guidorzi, C., Frontera, F., Valle, M. D., Finelli, F., Landi, R., & Montanari, E. 2008, *MNRAS*, 391, 577
- Amati, L., et al. 2002, *A&A*, 390, 81
- Barthelmy, S. D., et al. 2005, *Space Science Reviews*, 120, 143
- Bishop, C. M. 2006, *Pattern Recognition and Machine Learning (Information Science and Statistics)* (Secaucus, NJ, USA: Springer-Verlag New York, Inc.)
- Bloom, J. S., Frail, D. A., & Kulkarni, S. R. 2003, *ApJ*, 594, 674
- Bucciantini, N., Quataert, E., Arons, J., Metzger, B. D., & Thompson, T. A. 2008, *MNRAS: Letters*, 383, L25
- Bucciantini, N., Quataert, E., Metzger, B. D., Thompson, T. A., Arons, J., & Zanna, L. D. 2009, *MNRAS*, 396, 2038
- Burrows, D. N., et al. 2005, *Space Science Reviews*, 120, 165
- Cardone, V. F., Capozziello, S., & Dainotti, M. G. 2009, *MNRAS*, 400, 775
- Duncan, R. C., & Thompson, C. 1992, *AJ*, 392, L9
- Evans, P. A., et al. 2009, *MNRAS*, 397, 1177
- Fenimore, E. E., & Ramirez-Ruiz, E. 2000, eprint arXiv, 4176
- Frail, D. A., et al. 2001, *ApJ*, 562, L55
- Fraley, C., & Raftery, A. E. 2002, *Journal of the American Statistical Association*, 97, 611
- Fraley, C., Raftery, A. E., Murphy, T. B., & Scrucca, L. 2012, Technical Report 597, Department of Statistics, University of Washington (<http://www.stat.washington.edu/mclust/>)
- Ghirlanda, G., Ghisellini, G., & Firmani, C. 2006, *New Journal of Physics*, 8, 123
- Ghirlanda, G., Ghisellini, G., & Lazzati, D. 2004, *ApJ*, 616, 331
- Ghisellini, G., Nardini, M., Ghirlanda, G., & Celotti, A. 2009, *MNRAS*, 393, 253
- Hakkila, J., Giblin, T. W., Roiger, R. J., et al. 2003, *ApJ*, 582, 320
- Hakkila, J., Haglin, D. J., Pendleton, G. N., Mallozzi, R. S., Meegan, C. A., & Roiger, R. J. 2000, *ApJ*, 538, 165
- Horváth, I. 1998, *ApJ*, 508, 757
- Horváth, I., Bagoly, Z., Balázs, L. G., de Ugarte Postigo, A., Veres, P., & Mészáros, A. 2010, *ApJ*, 713, 552
- Horváth, I., Balázs, L. G., Bagoly, Z., Ryde, F., & Mészáros, A. 2006, *A&A*, 447, 23
- Horváth, I., Balázs, L. G., Bagoly, Z., & Veres, P. 2008, *A&A*, 489, L1
- Horváth, I. 2009, *Ap&SS*, 323, 83
- Kocevski, D. 2012, *Proceedings of the Gamma-Ray Bursts 2012 Conference (GRB 2012)*. May 7-11, 17
- Kodama, Y., Yonetoku, D., Murakami, T., Tanabe, S., Tsutsui, R., & Nakamura, T. 2008, *MNRAS: Letters*, 391, L1
- Liang, E., & Zhang, B. 2005, *ApJ*, 633, 611
- Liang, N., Xiao, W. K., Liu, Y., & Zhang, S. N. 2008 *ApJ*, 685, 354
- López-Cámara, D., Lee, W. H., & Ramirez-Ruiz, E. 2010, *ApJ*, 716, 1308
- MacFadyen, A. I., & Woosley, S. E. 1999, *ApJ*, 524, 262

- Metzger, B. D., Giannios, D., Thompson, T. A., Bucciantini, N., & Quataert, E. 2011, *MNRAS*, 413, 2031
- Mukherjee, S., Feigelson, E. D., Babu, G. J., Murtagh, F., Fraley, C., & Raftery, A. 1998, *ApJ*, 508, 314
- Nagataki, S. 2011, *PASJ*, 63, 1243
- Nousek, J. A., et al. 2006, *ApJ*, 642, 389
- Panaitescu, A., Mészáros, P., Burrows, D., Nousek, J., Gehrels, N., O’Brien, P., & Willingale, R. 2006, *MNRAS*, 369, 2059
- Proga, D., & Begelman, M. C. 2003, *ApJ*, 592, 767
- Reichart, D. E., Lamb, D. Q., Fenimore, E. E., Ramirez-Ruiz, E., Cline, T. L., & Hurley, K. 2001, *ApJ*, 552, 57
- Rhoads, J. E. 1999, *ApJ*, 525, 737
- Roming, P. W. A., et al. 2005, *Space Science Reviews*, 120, 95
- Salvaterra, R., et al. 2012, *ApJ*, 749, 68
- Schaefer, B. E. 2007, *ApJ*, 660, 16
- Tsutsui, R., Nakamura, T., Yonetoku, D., Murakami, T., Kodama, Y., & Takahashi, K. 2009, *Journal of Cosmology and Astroparticle Physics*, 08, 015
- Tsutsui, R., Nakamura, T., Yonetoku, D., Takahashi, K., & Morihara, Y. 2012, eprint arXiv, 1205, 2954
- . 2013, *PASJ*, 65, 3
- Tsutsui, R., & Shigeyama, T. 2013, *PASJ*, 65, L3
- Usov, V. V. 1992, *Nature*, 357, 472
- Willingale, R., et al. 2007, *ApJ*, 662, 1093
- Woosley, S. E. 1993, *AJ*, 405, 273
- Yamazaki, R. 2009, *ApJLetters*, 690, L118
- Yonetoku, D., Murakami, T., Nakamura, T., Yamazaki, R., Inoue, A. K., & Ioka, K. 2004, *ApJ*, 609, 935
- Zhang, B., Fan, Y. Z., Dyks, J., Kobayashi, S., Mészáros, P., Burrows, D. N., Nousek, J. A., & Gehrels, N. 2006, *ApJ*, 642, 354